ACS APPLIED MATERIALS & INTERFACES

www.acsami.org

Research Article

DNA-Guided Multivalent Antibody Display Boosts the Targeting Performance of Therapeutic Nanovesicles

Jiyuan Wu, Xi Liu, Tenghui Ye, Xianghua Zhong, Qin Fu, Zhenzhen Wang,* and Peng Shi*

Cite This: *ACS Appl. Mater. Interfaces* 2025, 17, 54484−54495

Read Online

ACCESS | Metrics & More | Article Recommendations | Supporting Information

ABSTRACT: Nanovesicles (NVs) have recently gained increasing attention in biomedical applications as alternatives to extracellular vesicles. However, their clinical translation is hindered by limited targeting specificity toward diseased tissues. In this study, we present a DNA-mediated self-assembly strategy to construct multivalent antibody-modified nanovesicles (Multi-NVs) for enhanced targeted delivery. Our results demonstrated that Multi-NVs prepared from mesenchymal stromal cells exhibited robust and specific targeting capabilities, improved cellular uptake efficiency, and promoted endothelial angiogenic activity. Importantly, this modular strategy demonstrated broad applicability across multiple disease models, including acute lung injury (ALI) and acute kidney injury, where Multi-NVs achieved markedly improved tissue targeting. Therapeutically, Multi-NV treatment significantly reduced macrophage infiltration and alleviated lung tissue damage and oxidative stress in ALI, highlighting their potential for precision medicine and personalized therapeutic interventions.

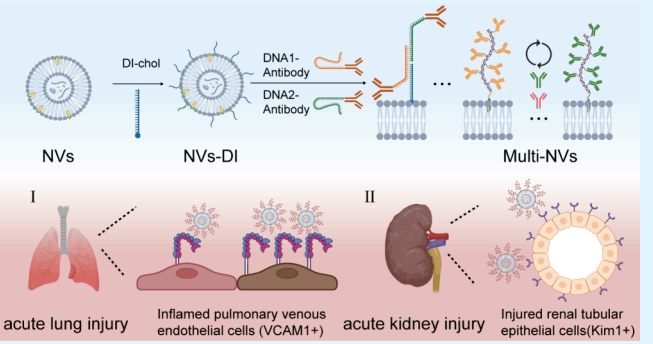

KEYWORDS: *DNA, self-assembly, biomolecular engineering, nanovesicle, mesenchymal stromal cells*

INTRODUCTION

In recent years, nanovesicles (NVs) have attracted considerable interest as alternative carriers to extracellular vesicles (EVs) for therapeutic applications.[1−3] NVs are exosome-mimetic structures generated either by serial mechanical extrusion of cells or by the hybridization of liposomes with natural exosomes.[4,5] They exhibit comparable particle sizes and membrane compositions to EVs, but offer markedly higher production yields and greater enrichment of proteins and RNAs.[2,6,7] These advantages have endowed NVs with broad potential across diverse biomedical applications.

However, despite these promising features, NVs—like their EV counterparts—exhibit limited in vivo targeting capabilities. This limitation is primarily attributed to the fact that NVs inherit certain membrane protein features from their parental cells.[8] As a result, unless derived from highly specialized cell types, most NVs lack the molecular specificity required for active homing to diseased tissues, thereby constraining their therapeutic potential.[9−12] To overcome this, current strategies for enhancing the targeting capabilities of NVs primarily rely on genetic engineering or chemical modification.[13] Genetic approaches typically involve expressing antibody fragments or specific receptors in source cells prior to extrusion, yielding NVs with surface-displayed targeting moieties.[14−18] While highly specific, these methods require labor-intensive plasmid construction, cell transfection, and prolonged screening, and transgene expression can be unstable and decline over time.[19,20] By contrast, chemical modification provides a more direct route, and recent advances—including copper-free click chemistry, bio-orthogonal click chemistry, enzyme-mediated conjugations, streptavidin−biotin coupling—have enabled antibodies, peptides, or aptamers to be attached to NV membranes with improved efficiency and reduced cytotoxicity.[21−25] These approaches can rapidly confer targeting capabilities without genetic manipulation. However, challenges remain, including the limited number of surface proteins on vesicles, which can lead to insufficient modification density, the risk that excessive alteration of surface proteins may impair the native functions of the vesicles, limited control over ligand orientation and density, and issues of scalability for clinical translation.[26,27] Therefore, the development of an efficient, controllable, and bioactivity-preserving strategy for functionalizing NVs remains a major technical bottleneck for advancing NV-based therapeutics.

Received: June 6, 2025
Revised: September 6, 2025
Accepted: September 9, 2025
Published: September 17, 2025

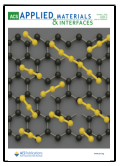

https://doi.org/10.1021/acsami.5c11126
ACS Appl. Mater. Interfaces 2025, 17, 54484−54495

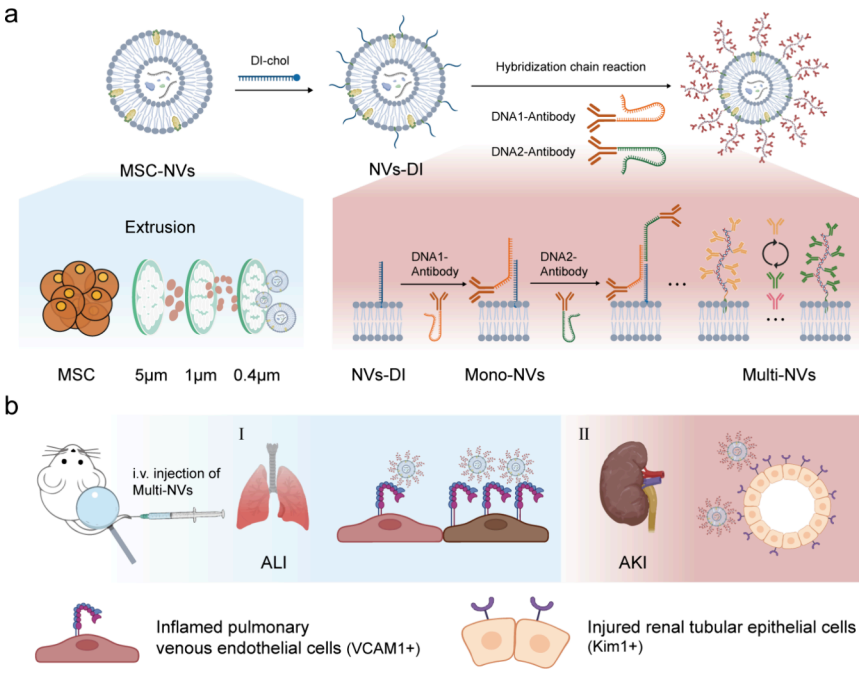

Figure 1. Schematic illustration of the preparation of Multi-NVs and their targeting of acute lung injury (ALI) and acute kidney injury (AKI) models. (a) Schematic preparation of Multi-NVs. After incubation with cholesterol-modified DNA initiator strand (DI-chol), NVs were subsequently assembled with DNA1-Antibody and DNA2-Antibody through a hybridization chain reaction (HCR) to form Multi-NVs. This modular strategy enables flexible customization of NVs by varying the DNA-antibody components to match different disease targets. (b) By selecting different targeting ligands such as vascular cell adhesion molecule-1 (VCAM1) and kidney injury molecule-1 (Kim1), the resulting Multi-NVs were able to selectively target inflamed pulmonary vascular endothelial cells and renal tubular epithelial cells. Image created by BioRender.com, with permission.

Here, we introduce a mild and versatile surface engineering approach based on biomolecular self-assembly to enhance the targeting capability of NVs. This approach involves conjugating DNA strands to antibodies, followed by the multivalent display of these antibodies on the NVs surface via DNA template-directed assembly (Figure 1a). This strategy offers several distinct advantages. It simplifies NVs modification to a two-step mixing procedure under physiological conditions, avoiding the need for genetic manipulation or harsh chemical treatments. Moreover, the multivalent display of antibodies enhances molecular recognition by providing abundant functional sites on the NVs surface. Additionally, the modular nature of this approach enables flexible customization of NVs for different therapeutic targets by simply exchanging the antibody component (Figure 1b). Mesenchymal stromal cell (MSC)-derived EVs are recognized for their remarkable biological functions, including immunomodulation, anti-inflammatory effects, and pro-angiogenic activity.[14,28,29] NVs derived from MSCs have similarly demonstrated significant potential in a variety of biomedical applications.[7,30,31] In this study, we used MSCs as the source for generating multivalent antibody-modified NVs (Multi-NVs). By employing different targeting antibodies, we achieved efficient targeting of Multi-NVs to inflamed vascular endothelial cells and injured renal tubular epithelial cells, leading to their effective accumulation in lung and kidney tissues. In a mouse model of acute pneumonia, we further confirmed that enhanced targeting of Multi-NVs significantly reduced alveolar macrophage levels and alleviated lung injury. These findings suggest that DNA template-directed antibody assembly offers a versatile and clinically translatable platform for engineering NVs toward precision medicine applications.

RESULTS AND DISCUSSION

Construction of Multivalent Antibodies on the Surface of Nanovesicles. In this study, Multi-NVs and monovalent antibody-modified NVs (Mono-NVs) were prepared via DNA template-directed assembly (Figure 2a). We first prepared MSC-derived NVs by serial mechanical extrusion of cells and confirmed that the protein profiles of NVs closely resembled those of their parental MSCs (Figure 2b). To enable multivalent antibody display on the NV surface, we employed a rationally designed DNA self-assembly system. This system comprised a cholesterol- modified DNA initiator strand (DI-chol) and two DNA-antibody conjugates, DNA1-antibody and DNA2-antibody. In the presence of DI-chol, DNA1-antibody and DNA2-antibody underwent a hybridization chain reaction to form a multivalent antibody structure (Figure S1a). As a proof of concept, we used IgG labeled with fluorescein isothiocyanate (IgG-FITC) as a model antibody to validate the formation of these multivalent structures. DNA-IgG conjugates were generated using SoluLINK Bioconjugation Reagents, with successful conjugation confirmed via UV–Vis spectroscopy and SDS-PAGE analysis (Figure S2). Subsequent gel electrophoresis further demonstrated that DNA1-IgG and DNA2-IgG self-assembled into high-molecular-weight antibody polymers in the presence of DI-chol (Figure S1b), confirming the capability of the system to support multivalent antibody assembly.

Next, we applied this DNA self-assembly system to construct multivalent IgG structures on NV surfaces. DI-chol was first anchored to the NV membrane via hydrophobic interactions, followed by the addition of DNA1-IgG and DNA2-IgG to facilitate the antibody assembly. Confocal microscopy revealed strong fluorescence colocalization between the NV membrane

https://doi.org/10.1021/acsami.5c11126
ACS Appl. Mater. Interfaces 2025, 17, 54484−54495

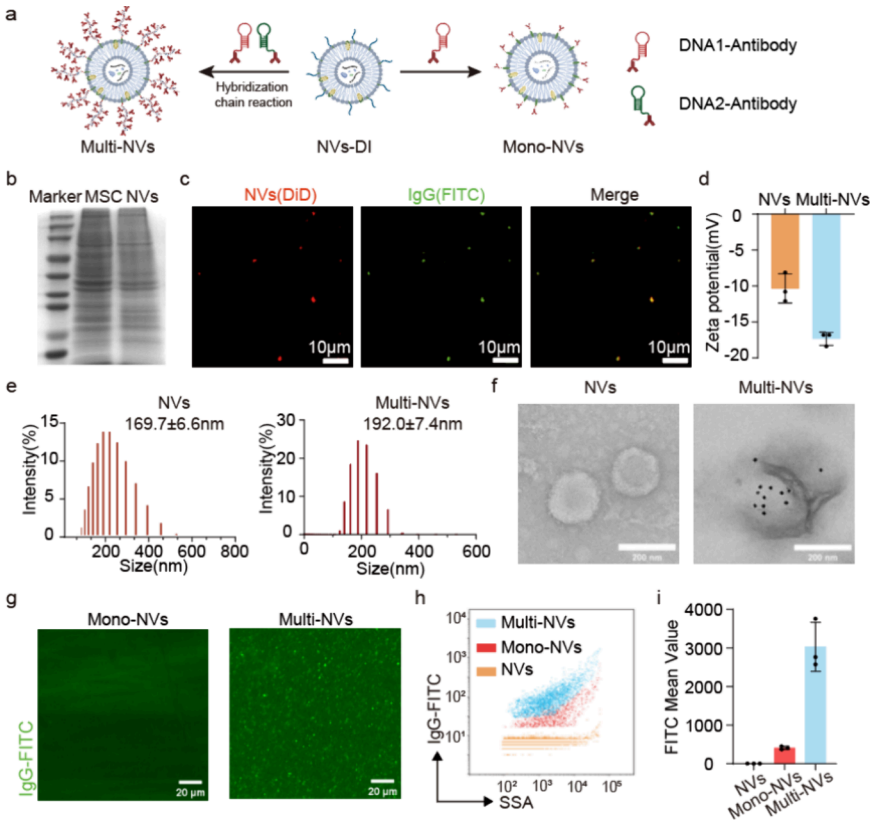

Figure 2. Preparation and characterization of Multi-NVs. (a) Schematic illustration of the preparation of Multi-NVs and Mono-NVs. (b) Sodium dodecyl sulfate-polyacrylamide gel electrophoresis (SDS−PAGE) pattern of proteins from MSC and NVs. (c) Confocal fluorescence images of Multi-NVs. Scale bar, 10 μm. (d) Zeta potential measurements of NVs and Multi-NVs. (e) Size distribution profiles of NVs and Multi-NVs. (f) TEM images showing immunogold-labeled secondary antibodies bound to the surface of Multi-NVs. The gold nanoparticles appear as black dots indicating antibody localization. Scale bar, 200 nm. (g) Fluorescence microscopy images of Multi-NVs and Mono-NVs. Scale bar, 20 μm. (h) Nanoflow cytometry analysis of the fluorescence intensity of Mono-NVs and Multi-NVs. (i) Quantification of the mean fluorescence intensity shown in (h). Data are presented as mean ± standard deviation (SD) (n = 3).

dye DiD and DNA-IgG-FITC (Figure 2c), confirming successful surface modification. This was further supported by a decrease in surface zeta potential from −10.02 mV for unmodified NVs to −17.33 mV for Multi- NVs (Figure 2d). Moreover, dynamic light scattering (DLS) analysis revealed an increase in hydrodynamic diameter from 169 to 192 nm after DNA-IgG assembly (Figure 2e). Transmission electron microscopy (TEM) revealed binding of immunogold-labeled secondary antibodies to Multi-NVs (Figure 2f), further supporting the successful antibody functionalization of the NV surfaces. Next, the antibody binding capacity of Multi-NVs was determined to be 24 ng per μg of NVs (Figure S3). To highlight the impact of multivalency, we constructed Mono-NVs by incubating DI-chol-modified NVs with DNA1-IgG alone. Fluorescence microscopy revealed that Multi-NVs exhibited markedly stronger fluorescence signals and more clearly defined vesicular structures compared to Mono-NVs (Figure 2g). Nanoflow cytometry further demonstrated a 7-fold increase in fluorescence intensity for Multi-NVs relative to Mono-NVs (Figure 2h,i). Together, these results confirm that the DNA self-assembly strategy successfully enabled the multivalent decoration of NVs with antibodies.

To evaluate the stability of Multi-NVs, we prepared Multi-NVs modified with DNA-IgG-FITC and incubated them in 10% FBS. After 24 h, Multi-NVs retained 62.2% of their fluorescence intensity (Figure S4a,b).[32] Consistently, DLS analysis indicated that their hydrodynamic diameter remained stable over the same period (Figure S4c). Collectively, these findings demonstrate that the DNA-mediated surface engineering strategy not only enables efficient multivalent antibody display but also preserves the physicochemical stability of NVs, supporting their potential for in vivo therapeutic applications.

In Vitro Targeting Properties of Multi-NVs. To evaluate the targeting capability of Multi-NVs, we selected vascular cell adhesion molecule 1 (VCAM1), which is highly expressed on endothelial cells under inflammatory conditions, as the model target. Accordingly, DNA-anti-VCAM1 conjugates were prepared and assembled onto NVs to generate Multi-NVs. We first verified that DNA conjugation did not impair the target specificity of anti-VCAM1 by incubating DNA-anti-VCAM1 with VCAM1-positive mouse endothelial cells (C166 cell line) and VCAM1-negative HeLa cells. Flow cytometry confirmed preserved recognition specificity (Figure S5). Subsequently, DiD-labeled Multi-NVs were incubated with C166 and HeLa cells. Fluorescence microscopy demonstrated that Multi-NVs specifically bound to the membranes of C166 cells while exhibiting negligible binding to HeLa cell membranes (Figure 3a). Notably, flow cytometry analysis demonstrated that C166 cells exhibited approximately an 8-fold higher DiD-positive rate than HeLa cells (Figure 3b,c). These results indicate that the multivalent anti-VCAM1 displayed on the NVs surface retained its specific recognition ability, enabling targeted delivery of NVs to the intended cells.

https://doi.org/10.1021/acsami.5c11126
ACS Appl. Mater. Interfaces 2025, 17, 54484−54495

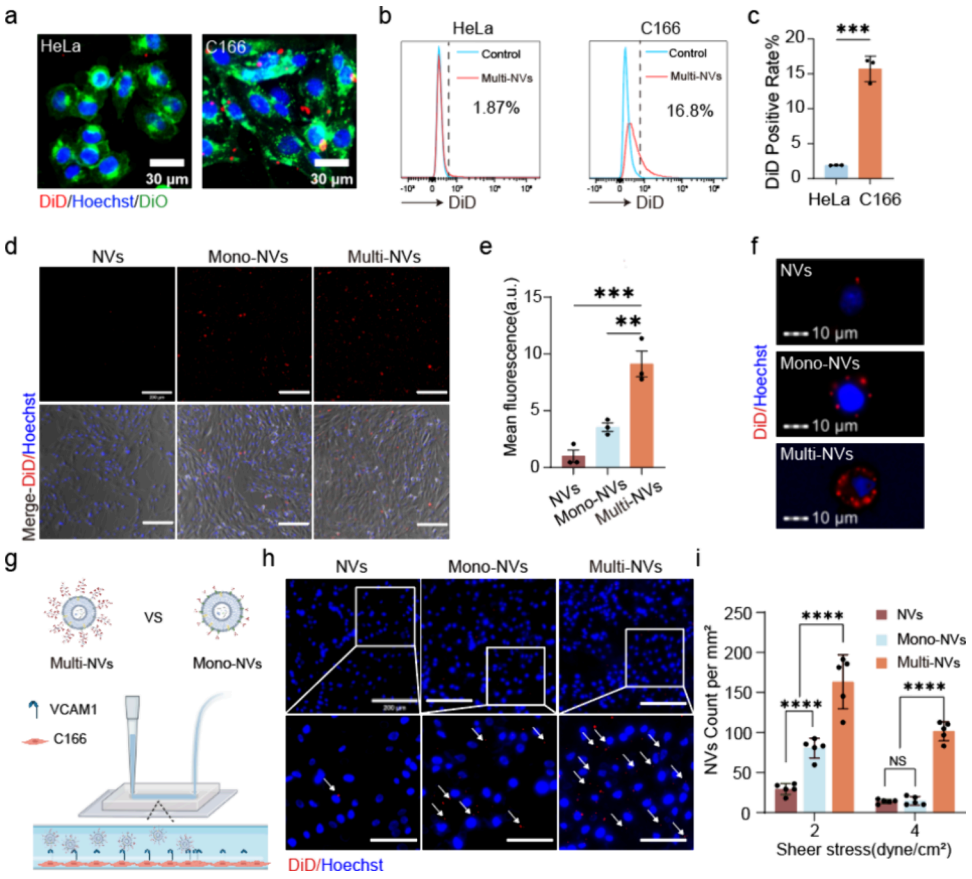

Figure 3. In vitro targeting ability of engineered NVs. (a) Confocal fluorescence images showing colocalization of Multi-NVs with the cell membrane in HeLa and C166 cells. Scale bar, 30 μm. (b) Flow cytometry analysis of C166 and HeLa cells incubated with Multi-NVs. (c) Quantification of DiD-positive proportions of C166 and HeLa cells from panel (b) (n = 3). (d) Fluorescence microscopy images showing static adhesion of engineered NVs (red) to C166 cells (blue). Scale bar, 200 μm. (e) Quantification of NVs fluorescence intensity in panel (d) (n = 3). (f) Imaging flow cytometry analysis of engineered NVs adhesion to C166 cells. Scale bar, 10 μm. (g) Schematic representation of the flow adhesion assay using a microfluidic chip. (h) Representative images of engineered NVs adhesion to cells under a shear force of 2 dyn/cm^2. Arrows mark representative vesicles bound to the cell membrane. Scale bar, 200 μm. (i) Quantification of the number of vesicles adhered to C166 cell surfaces under shear forces of 2/4 dyn/cm^2 using ImageJ (n = 5). Red fluorescence indicates DiD labeled NVs, while blue fluorescence represents Hoechst-stained nuclei, and green fluorescence corresponds to DiO-stained cell membranes. Data are presented as mean ± SD, and statistical significance was calculated using one-way ANOVA followed by Tukey's post hoc test. **p < 0.01, ***p < 0.001, ****p < 0.0001 indicate significant differences at various levels of significance.

Unlike conventional monovalent antibody modifications, our DNA-mediated self-assembly approach enables high-density antibody anchoring on the NV surface, which is expected to significantly enhance targeting performance.[33,34] To test this, we compared the adhesion of Multi-NVs, Mono-NVs, and unmodified NVs to C166 cells under static conditions. Fluorescence microscopy revealed that Multi-NVs exhibited the highest adhesion density to C166 cells (Figure 3d). Quantitative analysis showed that the mean fluorescence intensity of Multi-NVs bound to C166 cells was 3.5-fold and 9.1-fold greater than that of Mono-NVs and NVs, respectively (Figure 3e). Imaging flow cytometry further confirmed that Multi-NVs achieved the highest number of adhesion events on the cell surface (Figure 3f). To better mimic the hemodynamic environment in vivo, we employed a microfluidic chip system capable of controlling shear stress (Figure 3g). This setup allowed different types of NVs to flow across C166 cells under defined shear conditions. The results demonstrated that Multi-NVs consistently exhibited superior adhesion to C166 cells compared to Mono-NVs under all tested shear stress conditions. Notably, the adhesion density ratio of Multi-NVs to Mono-NVs increased from approximately 2-fold at 2 dyn/cm^2 to 10-fold at 4 dyn/cm^2 (Figure 3h,i), strongly indicating that the multivalent antibody structure substantially improves NVs adhesion under dynamic flow conditions.

Multivalent Modification Promotes NV Internalization and Angiogenic Function. Having demonstrated enhanced binding, we next investigated whether multivalent modification also improved NVs internalization. Confocal fluorescence imaging showed efficient uptake of Multi-NVs by C166 cells, with strong vesicular fluorescence signals distributed throughout the cytoplasm and perinuclear regions (Figure 4a,b). Time-course flow cytometry analysis revealed that Multi-NVs achieved the highest uptake rates at all measured time points (1, 4, and 8 h) (Figure 4c–e). Remarkably, at 4 h, the uptake rate of Multi-NVs reached 59.3%, surpassing the maximum uptake rates observed at 8 h for Mono-NVs (58.6%) and NVs (34%) (Figure 4f). These results indicate that Multi-NVs achieve more rapid and efficient cellular internalization compared to Mono-NVs and NVs. Confocal imaging further confirmed this finding, showing that the intracellular accumulation of Multi-NVs was both

https://doi.org/10.1021/acsami.5c11126
ACS Appl. Mater. Interfaces 2025, 17, 54484−54495

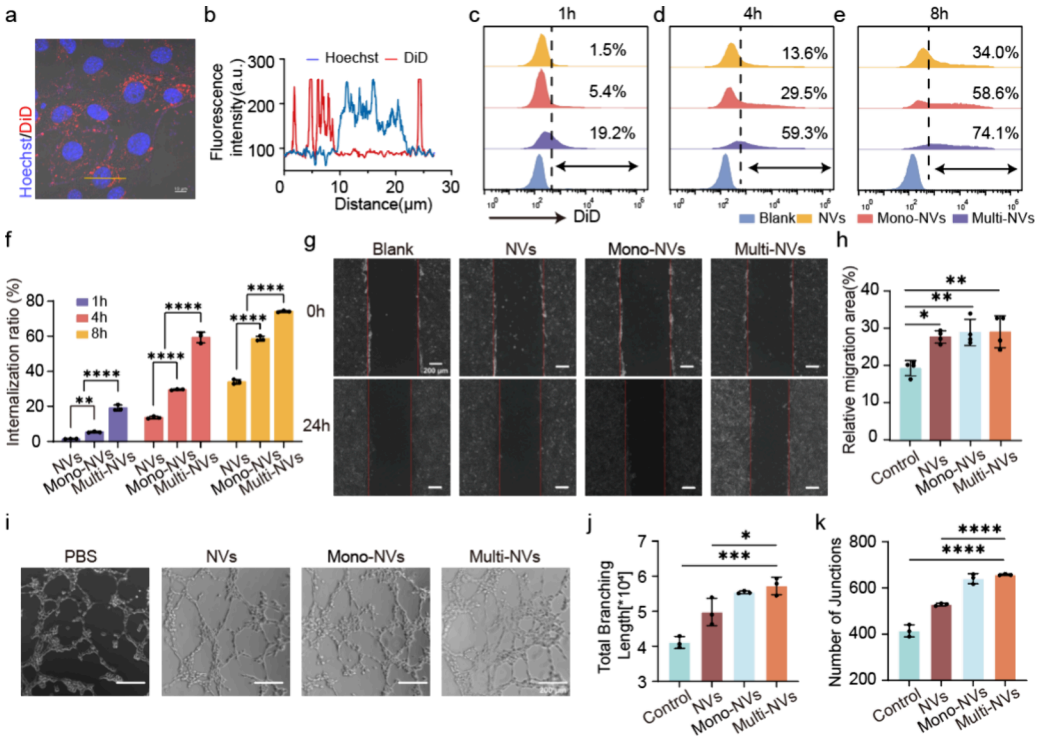

Figure 4. In vitro functional validation of engineered NVs. (a) Confocal microscopy images showing the uptake of Multi-NVs by C166 cells. Scale bar, 10 μm. (b) Fluorescence intensity profile along the orange line in panel (a). (c–e) Flow cytometry analysis of C166 cells following incubation with engineered NVs for 1, 4, and 8 h, respectively. (f) Quantification of flow cytometry data from panels (c–e) (n = 3). (g) Migration of C166 cells after 24 h of treatment with engineered NVs; red lines indicate the boundary of the cell-free area. Scale bar, 200 μm. (h) Quantification of the cell migration rate shown in panel (g) (n = 4). (i) Representative images of tube formation by C166 cells treated with engineered NVs. (j,k) Quantitative analysis of the tube formation assay (n = 3). Scale bar, 200 μm. All data are presented as mean ± SD, and statistical significance was determined by one-way ANOVA followed by Tukey's post hoc test. *p < 0.05, **p < 0.01, ***p < 0.001, ****p < 0.0001 indicate statistically significant differences at varying levels.

faster and more pronounced than that of the control groups (Figure S6). We further validated that this enhanced uptake behavior was primarily driven by the Anti-VCAM1 moiety rather than changes in zeta potential or particle size (Figure S7). Collectively, these data demonstrate that multivalent antibody modification significantly enhances both cellular binding and internalization efficiency of NVs.

To evaluate the functional consequences of this enhanced uptake, we assessed the effects of Multi-NVs on cell proliferation, angiogenesis, and migration. Based on preliminary cytotoxicity assessments, 10 μg/mL was selected as the working concentration of NVs (Figure S8a). In proliferation assays, NVs, Mono-NVs, and Multi-NVs all significantly promoted C166 cell proliferation, with no notable differences among the three groups, indicating that antibody modification did not interfere with the inherent proliferative capacity of NVs (Figure S8b). Cell migration assays demonstrated that all three types of NVs effectively promoted C166 cell migration (Figure 4g,h). Moreover, in angiogenesis assays, Multi-NVs markedly enhanced the formation of vascular nodes and total vessel length compared to NVs and the untreated group, likely due to their higher cellular uptake (Figure 4i–k). Taken together, these results indicate that multivalent antibody modification preserves the intrinsic bioactivity of NVs and may further potentiate angiogenesis through improved cellular delivery.

In Vivo Targeting Properties of Multi-NVs. Encouraged by the promising in vitro findings, we next assessed the in vivo targeting performance of Multi-NVs using a murine model of acute lung injury (ALI), a clinically relevant condition characterized by pronounced pulmonary inflammation and VCAM1 upregulation.[35] ALI was induced via intratracheal administration of lipopolysaccharide (LPS), which resulted in visible pulmonary edema and hemorrhage within 4 h (Figure S9a,b), and was further validated by H&E staining showing diffuse interstitial edema (Figure S9c). DiD-labeled Multi-NVs, Mono-NVs, and NVs were then intravenously injected into ALI mice. Major organs were collected at 2, 14, and 24 h postinjection for fluorescence imaging to evaluate the biodistribution of NVs (Figure 5a). At 2 h, Multi-NVs exhibited significantly higher accumulation in the lungs compared to NVs and Mono-NVs (Figure 5b), with a 7-fold increase in fluorescence intensity relative to NVs (Figure 5c). Over time, the lung fluorescence signal decreased as NVs redistributed to the liver, spleen, and kidneys for clearance (Figure S10).[36,37] Furthermore, immunofluorescence staining of lung tissues at 2 h revealed that engineered NVs were colocalized with the inflamed pulmonary vasculature, with Multi-NVs exhibiting greater adhesion compared to NVs and Mono-NVs (Figure 5d,e). These findings highlight the superior pulmonary targeting efficiency of Multi-NVs in vivo.

To test the generalizability of this targeting strategy, we extended our evaluation to a second disease model: acute kidney injury (AKI), a condition frequently encountered in critically ill patients (Figure 5f). AKI progression is associated with renal tubular epithelial cell apoptosis and elevated expression of kidney injury molecule-1 (Kim-1), a specific biomarker of tubular damage.[38,39] Accordingly, we engineered Multi-NVs using anti-Kim-1 antibodies to enable targeted renal

https://doi.org/10.1021/acsami.5c11126
ACS Appl. Mater. Interfaces 2025, 17, 54484–54495

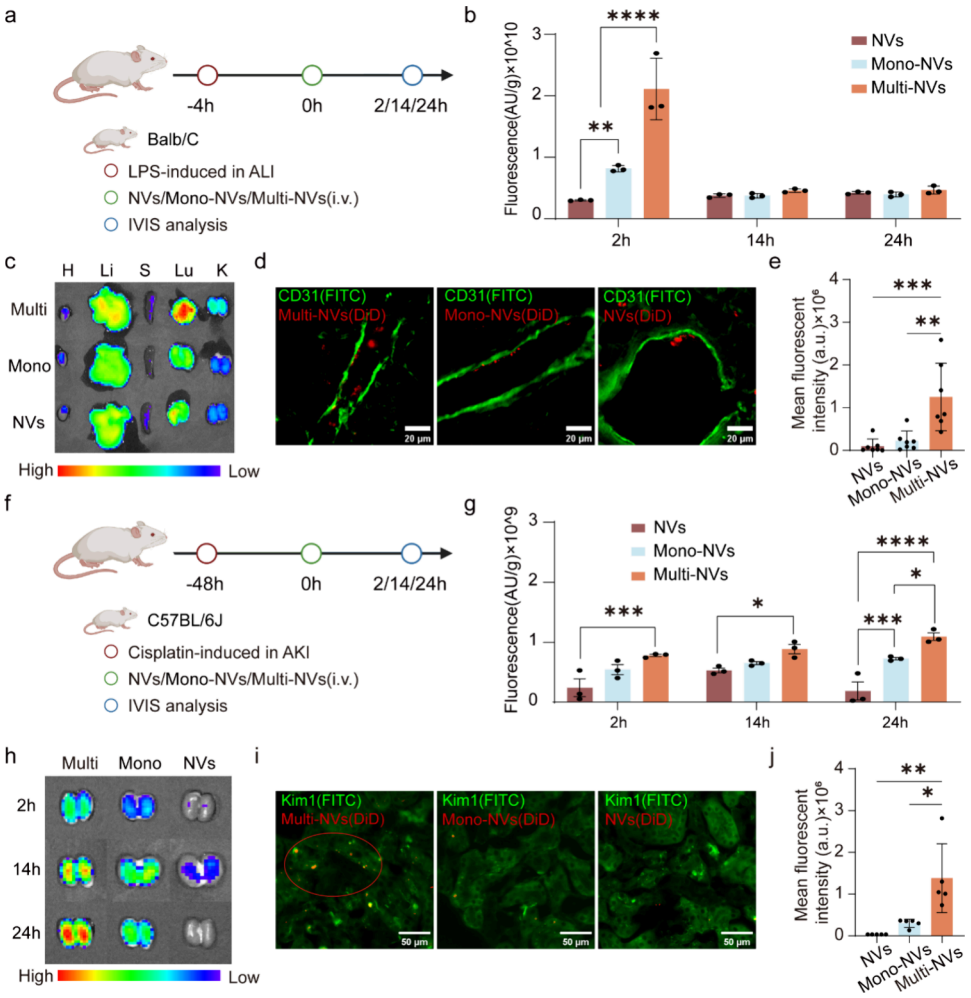

Figure 5. In vivo targeting ability of engineered NVs. (a) Schematic illustration of the experimental design for evaluating the targeting ability of engineered NVs in an ALI model. (b) Quantification of lung fluorescence intensity at different time points (n = 3). (c) Representative IVIS images showing the distribution of NVs in major organs 2 h postinjection. (d) Representative immunofluorescence images of lung tissue sections 2 h after intravenous injection of engineered NVs. Scale bar, 20 μm. (e) Quantification of NVs fluorescence intensity in lung sections from each group (n = 7). (f) Schematic illustration of the experimental design for evaluating the targeting ability of engineered NVs in an AKI model. (g) Quantification of kidney fluorescence intensity at different time points (n = 3). (h) Representative ex vivo fluorescence images of kidneys 2, 14, and 24 h after injection of engineered NVs. (i) Representative immunofluorescence images of kidney tissue sections 24 h after intravenous injection of engineered NVs. Scale bar, 50 μm. (j) Quantification of NVs fluorescence intensity in kidney sections from each group (n = 5). All data are presented as mean ± SD, and statistical significance was determined by one-way ANOVA followed by Tukey's post hoc test. *p < 0.05, **p < 0.01, ***p < 0.001, ****p < 0.0001 indicate statistically significant differences at varying levels. Organ abbreviations: H, heart; Li, liver; S, spleen; Lu, lung; K, kidney.

delivery. Active ingredient-induced AKI was establishe in C5 mice via intraperitoneal injection (20 mg/kg), and Kim-1 over-expression in renal tissues was confirmed by immun ofluor-escence (Figure S11). Following intravenous administrat ion of engineered NVs, ex vivo kidney imaging at 2, 14, an d 24 h revealed significantly higher accumulation of Mul ti-NVs compared to controls, with a 5.8-fold increase in fluore scence intensity at 24 h (Figure 5g,h). Histological analysis f urther showed prominent accumulation of Multi-NVs in injure d renal tubular regions (Figure 5i,j). These results demonstra te the adaptability of our multivalent engineering approach a nd its efficacy in targeting different disease-relevant tissues.

Therapeutic Efficacy of Multi-NVs against ALI. Encouraged by the excellent in vivo targeting performance of Multi-NVs, we investigated whether the enhanced targeting capability of Multi-NVs translated into improved therapeutic outcomes in the ALI model. Macrophages are key mediators of inflammation in ALI, therefore, we analyzed macrophage infiltration in the alveolar regions across different treatment groups. Flow cytometry analysis revealed that in the untreated ALI group, the proportion of alveolar macrophages dramatically increased from 13.86 to 59.4%. In contrast, treatment with NVs and Mono-NVs moderately improved macrophage infiltration. Notably, Multi-NVs treatment significantly reduced macrophage infiltration in the alveoli compared to other treatment groups (Figures S12 and 6a,b). Quantitative PCR analysis revealed that Multi-NVs most effectively suppressed IL-6 and TNF-α expression while markedly enhancing IL-10 expression (Figure 6c−e). Multi-NVs alleviated alveolar macrophage infiltration and modulated the expression of associated inflammatory cytokines, which was potentially accompanied by a reduction in oxidative stress. Consistently, we further demonstrated that Multi-NVs significantly decreased the levels of 8-hydroxy-2′-deoxyguanosine (8-OHdG), a well-established marker of oxidative DNA damage, in lung tissues, indicating an attenuation of oxidative injury (Figure

https://doi.org/10.1021/acsami.5c11126
ACS Appl. Mater. Interfaces 2025, 17, 54484−54495

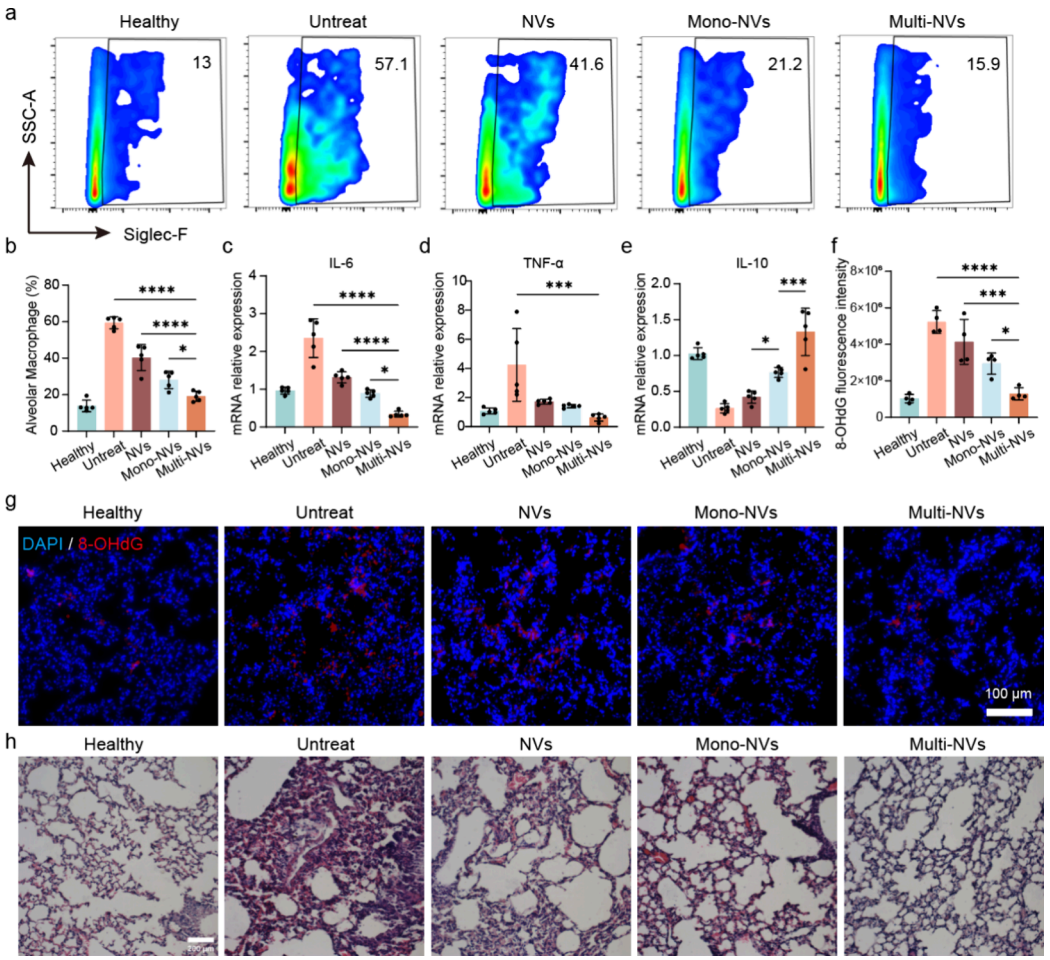

Figure 6. Multi-NVs attenuate alveolar macrophage infiltration and oxidative stress in a mouse model of ALI. (a) Representative flow cytometry plots showing the frequency of alveolar macrophage among CD11c+CD11b-cells after different treatments. (b) Quantification of alveolar macrophage proportions from panel (a) (n = 5). (c−e) mRNA expression levels of pro-inflammatory cytokines IL-6 (c) and TNF-α (d), and the anti-inflammatory cytokine IL-10 (e) in lung tissue homogenates following the indicated treatments (n = 5). (f) Quantification of fluorescence intensity from panel (g) (n = 4). (g) Representative immunofluorescence images of lung tissue sections stained for the oxidative stress marker 8-OHdG. Scale bar, 100 μm. (h) Representative hematoxylin and eosin (H&E)-stained images of lung tissue sections from experimental groups. Scale bar, 200 μm. All data are presented as mean ± SD, and statistical significance was determined by one-way ANOVA followed by Tukey's post hoc test. *p < 0.05, ***p < 0.001, ****p < 0.0001 indicate statistically significant differences at varying levels.

6f,g). Additionally, histological analysis demonstrated that Multi-NVs significantly reduced pulmonary edema and attenuated lung injury. (Figure 6h). These results suggest that Multi-NVs effectively modulate macrophage accumulation in the alveolar region and alleviate lung inflammation. No obvious histopathological alterations were detected in other major organs (Figure S13a), and hematological indices (Table S1) as well as biochemical markers of liver and kidney function were within normal limits (Figure S13b), indicating that Multi-NVs possess favorable biocompatibility in vivo. Together, these findings demonstrate that multivalent antibody modification substantially enhances both the targeting and therapeutic efficacy of NVs in inflammatory disease models.

CONCLUSIONS

In summary, we have developed a DNA-mediated self-assembly strategy for NVs surface engineering, enabling gentle assembly of antibodies on the NVs surface and convenient exchange of targeting ligands for precise and efficient tissue-specific delivery. Our results demonstrate that Multi-NVs exhibit excellent in vitro targeting specificity, rapid cellular uptake, and enhanced biological activities, including proliferation, migration, and angiogenesis. Importantly, Multi-NVs successfully targeted inflamed vasculature in ALI model and renal tubular epithelial cells in AKI model, validating their in vivo applicability. Furthermore, Multi-NVs treatment significantly reduced alveolar macrophage infiltration, mitigated lung tissue damage, and showed favorable biocompatibility in the ALI model, underscoring their therapeutic potential. These findings highlight the potential of the multivalent engineering strategy to advance NV-based precision medicine and personalized therapeutic interventions, offering a more efficient and customizable platform for future clinical applications.

METHODS AND MATERIALS

Materials. Oligonucleotides (Table S2) were synthesized by Sangon Biotech Co., Ltd. (Shanghai, China). The SDS-PAGE Preparation Kit was also obtained from Sangon Biotech. Cell Counting Kit-8, DiD cell-labeling solution, and Matrix-Gel Basement Membrane Matrix (Cat. No. C0372) were purchased from Beyotime Biotechnology Co., Ltd. (Shanghai, China). Dulbecco's Modified Eagle's Medium (DMEM, high

https://doi.org/10.1021/acsami.5c11126
ACS Appl. Mater. Interfaces 2025, 17, 54484−54495

glucose), trypsin−EDTA, and active ingredient−active ingredient was obtained from Gibco (Life Technologies, Carlsbad, CA, USA). Fetal bovine serum (FBSwas purchased from Biological Industries (Cat. No. 04-001ACS). Gold nanoparticles (Cat.No. BS-0293R-Gold) were purchased from Bioss (Beijing,China). Flow cytometry antibodies, including FITC antimouse VCAM1 (Cat. No. 105706), Ultra-LEAF antimouse VCAM1 (Cat. No. 105728), FITC antimouse CD31 (Cat. No.102506), antimouse KIM1 (Cat. No. B-305322), PE/Cy7 anti-CD11b (Cat. No. 101215), APC anti-Siglec-F (Cat. No.155507), BC421 anti-CD45 (Cat. No. 147719), and BV605 anti-CD11c (Cat. No. 117333), were obtained from BioLegend. Anti-8-OHdG were obtained from MedChemExpress. Conjugation of DNA to antibodies was performed using SoluLink bioconjugation technology. The S-4FB Cross-linker (Cat. No. S-1004-010), S-HyNic Cross-linker (Cat. No. S-1002-105), and TurboLink Catalyst Buffer (Cat. No. S-2006-105) were purchased from SoluLink.

Cell Culture. BMSC, C166 cells, and HeLa cells were purchased from iCell Bioscience Co., Ltd. (Shanghai, China).They were cultured in DMEM supplemented with 10% (v/v)FBS and 1% (v/v) active ingredient/active ingredient. All cultures were maintained at 37 °C in a humidified incubator with 5% CO_2.

Animal Treatments. Female BALB/c mice and male C57BL/6 mice were bought from GemPharmatech Co., Ltd. and housed in specified pathogen-free (SPF) animal facilities. All animal procedures were conducted in accordance with institutional guidelines and approved by the South China University of Technology Animal Care and Use Committee (Approval No. 2022020). All efforts were made to minimize animal suffering and to reduce the number of animals used.

Synthesis and Characterization of DNA-Antibody. Using the commercial SoluLink bioconjugation technology, DNA1 modified with an amino group at the 5′ end and DNA2 modified with an amino group at the 3′ end (Table S2) were reacted with S-4FB (N-succinimidyl-4-formylbenzoate) through the primary amines on the oligonucleotides to introduce a 4FB (4-formylbenzoate) linker. For the antibody, succinimidyl-6-hydrazinonicotinamide (S-HyNic) was used to introduce a 6-hydrazinonicotinamide (HyNic) group.[34] Then, the two were reacted in a specific Turbolink Catalyst Buffer for 2 h. Finally, the DNA-antibody was purified by ultrafiltration centrifugation. The concentration of the conjugate can be determined by measuring the absorbance of the bond (bisarylhydrazone) at 354 nm using UV.

Preparation and Characterization of NVs. NVs were prepared and purified by extrusion through polycarbonate membranes with different pore sizes. Briefly, MSCs (8×10^6) were resuspended in 1 mL of phosphate-buffered saline (PBS) and extruded using a mini-liposome extruder (HandExtruder, Genizer, USA) through polycarbonate membranes with pore sizes of 5 μm, 1 μm, and 400 nm. The extrusion was repeated 11 times back and forth for each membrane pore size. After extrusion, the vesicles were filtered through a 0.22 μm filter using a syringe to remove large vesicles and cell debris. The mimetic vesicles were washed by ultracentrifugation with a certain amount of PBS at 4 °C, at 100,000 g for 70 min at 4 °C, and the washing process was repeated twice. The washed NVs were aliquoted and stored at −80 °C.

Preparation and Characterization of Multi-NVs. To prepare Multi-NVs, NVs were resuspended in PBS at a concentration of 300 μg/mL. A cholesterol-modified DNA initiator strand (DI-chol) was added to the NVs suspension at a final concentration of 1 μM, followed by incubation at room temperature for 30 min. The mixture was then ultracentrifuged at 100,000 × g to remove unbound DI-chol, and the pellet was resuspended in PBS to yield DI-chol-modified NVs (NVs-DI).

For multivalent antibody assembly, DNA1-IgG and DNA2-IgG conjugates were mixed at a 1:1 molar ratio, each at a concentration of 0.5 μM, and incubated overnight at 4 °C to allow hybridization. The resulting antibody−DNA complexes were concentrated using centrifugal filtration with a 300 kDa molecular weight cutoff to obtain Multi-NVs. As a control, monovalent antibody-modified NVs (Mono-NVs) were prepared by incubating NVs-chol with DNA1-IgG alone under the same conditions. DiD/FITC colocalization was examined by confocal laser scanning microscopy (LSM 700, Carl Zeiss, Germany), and the fluorescence intensity of Multi-NVs and Mono-NVs was analyzed using a Flow NanoAnalyzer (nanoFACS, Xiamen, China).

Calculation of Antibody Loading. After assembly, Multi-NVs were washed multiple times using 300 kDa MWCO centrifugal filter units, and both filtrates and retentates were collected for analysis. Prepare a standard series of DNA−IgG−FITC dilutions in PBS (2, 3, 4, 5, 8, 10 ng IgG/μL). Measure fluorescence intensity in a black 96-well plate using a plate reader. Subtract background (PBS) signal and plot fluorescence vs IgG mass to generate a standard curve. Fit a linear regression and record the equation. Measure fluorescence intensity of each collected filtrate and an aliquot of the final retentate after appropriate dilution. Correct all readings by subtracting the PBS background. Convert fluorescence units to IgG mass using the standard curve equation.

Characterization of NVs and Multi-NVs. SDS−PAGE was performed to analyze the protein profiles of NVs and MSCs. The hydrodynamic particle sizes and zeta potentials of NVs and Multi-NVs were measured using a Malvern ZS90 particle size analyzer.

Multi-NVs were adsorbed on carbon-coated copper grids for 10 min, washed with PBS, and blocked with 5% BSA for 10 min. Grids were incubated with antibody-conjugated gold nanoparticles for 30 min at room temperature, washed, fixed with 0.25% glutaraldehyde, and stained with 2% uranyl acetate for 2 min. Samples were imaged by TEM.

The Multi-NVs were incubated in 10% (v/v) fetal bovine serum (FBS) at 37 °C for 0, 3, 6, 12, 24, and 48 h. At each time point, the samples were purified using 300 kDa ultrafiltration units to remove degraded components. The concentrated fractions were collected, and their fluorescence intensity was measured using a fluorescence spectrophotometer (F-7100, Hitachi High-Tech, Japan).

In Vitro Targeting Capability of Engineered NVs. To evaluate the specific targeting capability of Multi-NVs, C166 and HeLa cells were seeded in 24-well plates at a density of 2.5×10^4 cells per well and cultured for 24 h. Multi-NVs were resuspended in complete culture medium at a concentration of 10^9 particles/mL and incubated with the cells for 1 h. Following incubation, the cells were detached using 0.25% trypsin, washed twice with PBS, and stained for nuclei. Flow cytometry analysis was then performed to quantify cellular uptake. In parallel, cells were washed twice with PBS and fixed for observation under a fluorescence microscope.

To evaluate the enhanced targeting efficiency of Multi-NVs, DiD-labeled NVs, Mono-NVs, and Multi-NVs were resuspended in complete culture medium at a concentration of 10^9 particles/mL and incubated with C166 cells for 1 h. After

https://doi.org/10.1021/acsami.5c11126
ACS Appl. Mater. Interfaces 2025, 17, 54484−54495

incubation, the medium was removed, and the cells were washed three times with PBS. The nuclei were stained, and cellular uptake was visualized using a fluorescence microscope. In parallel, cells were detached using 0.25% trypsin, washed twice with PBS, and analyzed using an imaging flow cytometer to capture single-cell images. NVs were prelabeled with DiD before being used to construct Mono-NVs and Multi-NVs.

Targeting Efficiency of Engineered NVs toward C166 Cells under Different Shear Stress Conditions. Flow-based targeting assays were performed using ibidi microfluidic chambers (μ-Slide I 0.4 Luer, 80176, Germany). C166 cells were seeded into the chambers at a density of 2.5×10^6 cells/mL. Each channel was filled with 100 μL of culture medium to achieve an initial confluency of approximately 90%, followed by overnight incubation at 37 °C to reach full confluency.

Cells were stained with 1 × Hoechst 33342 (Beyotime) for 12 min, NVs, Mono-NVs, and Multi-NVs (equal particle numbers) were resuspended in 5 mL of cold PBS (4 °C) and injected into the microchannels at controlled flow rates using a precision syringe pump. The flow rates applied were 1 mL/min (corresponding to 2 or 4 dyn/cm^2) and 2 mL/min (corresponding to 8 dyn/cm^2). After flow application, the residual suspension was removed, and the channels were rinsed twice with PBS. Cell-associated red fluorescent signals (DiD-labeled nanovesicles) were visualized using a fluorescence microscope. The number of adhered NV particles per field was quantified using ImageJ software.

In Vitro Cellular Uptake of Multi-NVs. C166 cells were seeded at a density of 1.2×10^5 cells per 35 mm glass-bottom confocal dish (Nest, China) and cultured for 24 h at 37 °C in a humidified 5% CO_2 incubator. DiD-labeled Multi-NVs were added to the dishes and incubated with the cells for 8 h. After incubation, cells were fixed with 4% paraformaldehyde for 15 min at room temperature and washed three times with PBS. Cellular uptake of Multi-NVs was visualized using a confocal laser scanning microscope (Zeiss LSM 880, Germany).

Effect of Multivalent Antibody Modification on the Uptake Kinetics of NVs. To compare the time-dependent uptake efficiency of native and engineered NVs, vesicles were added at 0, 4, and 7 h prior to cell harvest, and analyzed at a fixed time point (8 h) by flow cytometry. The ratio of DiD-positive to DiD-negative cells was analyzed using flow cytometry (BD FACSVerse) to assess the cellular uptake efficiency of different NV formulations over time. The cellular uptake steps for Multi-NVs-IgG and Multi-NVs-VCAM1 were performed similarly.

Effect of Engineered NVs on Cell Viability. C166 cells were seeded into 96-well plates at a density of 5000 cells per well and cultured for 12 h. NVs were added at final concentrations of 10 μg/mL, 20 μg/mL, and 30 μg/mL, respectively, and incubated with the cells for 24 h. Cell viability was then assessed using the Cell Counting Kit-8 (CCK-8, Beyotime, China) according to the manufacturer's instructions. Based on the results, a concentration of 10 μg/mL NVs was selected for further testing. C166 cells were incubated with NVs, Mono-NVs, and Multi-NVs at 10 μg/mL for 24 h. Cell viability was again evaluated using the CCK-8 assay.

Promotion of Endothelial Cell Migration by Engineered NVs. C166 cells were seeded into 6-well plates at a density of 1×10^5 cells per well and cultured overnight to reach full confluence. A straight scratch was created across the center of each well using a 200 μL pipet tip, guided by a ruler to ensure consistency. Detached cells were removed by washing with PBS.

NVs, Mono-NVs, and Multi-NVs were each resuspended in culture medium containing 1% FBS at a concentration of 10 μg/mL and added to the wells. Cells were then incubated at 37 °C for 24 h.

After incubation, images of the scratched regions were acquired using an inverted fluorescence microscope (Nikon, Eclipse Ti2-E). Wound areas were quantified using ImageJ software, and the migration rate was calculated using the following formula:

$$\text{Migration rate (\%)} = (\text{initial wound size} - \text{wound size after 24 h}) / (\text{initial wound size}) \times 100\%$$

C166 Cell Angiogenesis Assay. The cell tube formation assay was performed using Matrigel to coat 96-well plates. C166 cells were mixed with engineered NVs and seeded onto the Matrigel-coated wells at a density of 50,000 cells per well. The cells were incubated for 4 h. For each group, five images were captured using an inverted microscope for statistical analysis. This translation accurately follows the original experimental setup, ensuring clarity, correctness, and logical flow.

Establishment of Acute Lung Injury and Acute Kidney Injury Models in Mice. To establish the ALI model, 6- to 8-week-old female BALB/c mice were anesthetized via intraperitoneal injection of active ingredient sodium.The anesthetized mice were placed on a tracheal intubation platform, and 40 μL of lipopolysaccharide (LPS, 10 mg/kg) was administered intratracheally. After instillation, mice were held in a vertical position and gently rotated to ensure uniform distribution of LPS throughout the lungs.

For the AKI model, 6- to 8-week-old male C57BL/6 mice were given a single intraperitoneal injection of active ingredient at a dose of 20 mg/kg (prepared as 1 mg/mL in normal saline). The AKI model was considered established 48 h postinjection. A total of 30 μg of NVs, Mono-NVs, or Multi-NVs was administered to model mice via tail vein injection.

Validation of Mouse ALI and AKI Models. To validate the ALI model, mouse lungs were harvested 4 h after intratracheal instillation of lipopolysaccharide (LPS). The wet weight of the lungs was recorded, followed by drying in a thermostatically controlled oven at 80 °C for 48 h until a constant weight was achieved. The lung wet-to-dry weight ratio was calculated using the formula: Wet/dry weight ratio = wet lung weight/dry lung weight.

Additionally, paraffin-embedded lung sections from both healthy and ALI mice were stained with hematoxylin and eosin (H&E) to examine histological changes and assess tissue damage. To validate the AKI model, kidney frozen sections were collected from healthy and AKI mice 2 days after active ing-r edient injection. Immunofluorescence staining for kidney injury molecule-1 (Kim-1) was performed to evaluate Kim-1 expression levels as a marker of renal injury.

Immunofluorescence Staining of Frozen Sections. Mouse lung and kidney tissues were fixed and cryosectioned at thicknesses of 8 and 7 μm, respectively. Tissue sections were mounted onto glass slides and dried in a slide dryer for 20 min. After drying, the sections were washed three times with PBS to remove residual fixative. The sections were then incubated

https://doi.org/10.1021/acsami.5c11126
ACS Appl. Mater. Interfaces 2025, 17, 54484−54495

with blocking buffer for 30−60 min at room temperature to prevent nonspecific binding. Primary antibodies were diluted in PBS, and applied to the sections to ensure complete coverage. The slides were placed in a humidified chamber and incubated overnight at 4 °C. Following primary antibody incubation, the slides were washed thoroughly with PBS to remove unbound antibodies. Appropriate fluorescent secondary antibodies were then applied, and the slides were incubated at room temperature for 60 min in the dark. Finally, the sections were washed, and imaged using a fluorescence microscope.

RNA Extraction and Quantitative Real-Time PCR Analysis of Lung Tissue. Total RNA was extracted from lung tissues using the Numspin RNA Quick Purification Kit (XinSaimei Biotechnology Co., Ltd., Cat. M5106). Genomic DNA was removed and reverse transcription performed using HiFiScript gDNA Removal RT MasterMix (Kangwei Century, Cat. CM2020M). Quantitative PCR was conducted in triplicate using MagicSYBR Mixture (Kangwei Century, Cat. CW3008M) on a LightCycler 96 (Roche). Cycling conditions were: 95 °C for 10 min; 40−45 cycles of 95 °C for 15 s and 60 °C for 30 s, followed by melt curve analysis. Relative gene expression was calculated by the $2^{-\Delta\Delta Ct}$ method with GAPDH as the internal control. Primer sequences are listed in Table S3.

Biocompatibility and Safety Evaluation. Histological analysis of major organs was performed using hematoxylin and eosin (H&E) staining. Serum samples were collected from treated animals to evaluate liver and kidney function by measuring the levels of aspartate aminotransferase (AST), alanine aminotransferase (ALT), and urea using standard clinical chemistry assays. Complete blood count (CBC) analysis was performed to comprehensively evaluate the physiological status and potential systemic toxicity of the mice.

Flow Cytometry Analysis. Mouse lungs were flushed with precooled PBS containing 1% fetal bovine serum (FBS) to collect bronchoalveolar lavage fluid (BALF). The collected BALF was centrifuged at 1600 rpm for 5 min at 4 °C to pellet the cells. The cell pellet was then resuspended in an appropriate buffer for subsequent flow cytometric analysis.

■ ASSOCIATED CONTENT

Supporting Information

The Supporting Information is available free of charge at https://pubs.acs.org/doi/10.1021/acsami.5c11126.

Assembly of multivalent antibodies (Figure S1); conjugation of DNA to IgG (Figure S2); quantification of antibody conjugation on Multi-NVs determined by ultrafiltration (Figure S3); stability analysis of Multi-NVs in 10% FBS (Figure S4); flow analysis of the specific binding of DNA-anti-VCAM1 to C166 cells and HeLa cells (Figure S5); confocal laser scanning microscopy (CLSM) images of C166 cells after incubation with NVs, Mono-NVs, and Multi-NVs for 1, 4, and 8 h (Figure S6); evaluation of surface property-dependent uptake of Multi-NVs by C166 cells (Figure S7); optimization of NV concentration and in vitro evaluation of proliferative effect of engineered NVs (Figure S8); evaluation of lung injury in LPS-treated and healthy mice (Figure S9); biodistribution of DiD-labeled NVs in major organs of mice with acute lung injury assessed at various time points (Figure S10); immunofluorescence staining of Kim1 in kidney sections from AKI and healthy mice (Figure S11); flow cytometry gating strategy for alveolar macrophages (Figure S12); safety assessments of NVs and engineered NVs in vivo (Figure S13); complete blood count analysis of mice 24 h after intravenous injection of NVs and engineered NVs (Table S1); DNA sequences used in this article (Table S2); and primers sequences for RT-qPCR in this study (Table S3) (PDF)

■ AUTHOR INFORMATION

Corresponding Authors

Zhenzhen Wang − *School of Biomedical Sciences and Engineering, South China University of Technology, Guangzhou 511442, P. R. China*; Email: zwang@scut.edu.cn

Peng Shi − *School of Biomedical Sciences and Engineering, South China University of Technology, Guangzhou 511442, P. R. China; National Engineering Research Center for Tissue Restoration and Reconstruction and Guangdong Provincial Key Laboratory of Biomedical Engineering, South China University of Technology, Guangzhou 510006, P. R. China*; orcid.org/0000-0002-8400-2358; Email: pxs301@scut.edu.cn

Authors

Jiyuan Wu − *School of Biomedical Sciences and Engineering, South China University of Technology, Guangzhou 511442, P. R. China*

Xi Liu − *School of Biomedical Sciences and Engineering, South China University of Technology, Guangzhou 511442, P. R. China*

Tenghui Ye − *School of Biomedical Sciences and Engineering, South China University of Technology, Guangzhou 511442, P. R. China*

Xianghua Zhong − *School of Biomedical Sciences and Engineering, South China University of Technology, Guangzhou 511442, P. R. China*

Qin Fu − *School of Biomedical Sciences and Engineering, South China University of Technology, Guangzhou 511442, P. R. China*

Complete contact information is available at: https://pubs.acs.org/10.1021/acsami.5c11126

Author Contributions

J.W. and X.L. contributed equally to this work. J.W. performed the experiments, interpreted the data, and wrote the manuscript. X.L. performed DNA-antibody conjugation and contributed to animal experiments. T.Y., X.Z., and Q.F. did experiments. Z.W. and P.S. supervised all experiments and revised the manuscript.

Notes

The authors declare no competing financial interest.

■ ACKNOWLEDGMENTS

This work was supported by the National Key R&D Program of China (2022YFB3808300), the National Natural Science Foundation of China (22277030), the Fundamental Research Funds for the Central Universities (2024ZYGXZR022), and the Guangzhou Basic and Applied Basic Research Foundation (SL2023A04J00706).

REFERENCES

(1) Zhang, Y.; Deng, Y.; Zhai, Y.; Li, Y.; Li, Y.; Li, J.; Gu, Y.; Li, S. A Bispecific Nanosystem Activates Endogenous Natural Killer Cells in the Bone Marrow for Haematologic Malignancies Therapy. *Nat. Nanotechnol.* **2024**, *19*, 1558−1568.

(2) Wang, X. Y.; Hu, S. Q.; Zhu, D. S.; Li, J. L.; Cheng, K.; Liu, G. Comparison of Extruded Cell Nanovesicles and Exosomes in Their Molecular Cargos and Regenerative Potentials. *Nano Res.* **2023**, *16*, 7248−7259.

(3) Lou, S.; Hu, W.; Wei, P.; He, D.; Fu, P.; Ding, K.; Chen, Z.; Dong, Z.; Zheng, J.; Wang, K. Artificial Nanovesicles Derived from Cells: A Promising Alternative to Extracellular Vesicles. *ACS Appl. Mater. Interfaces* **2025**, *17*, 22−41.

(4) Jiang, S.; Cai, G.; Yang, Z.; Shi, H.; Zeng, H.; Ye, Q.; Hu, Z.; Wang, Z. Biomimetic Nanovesicles as a Dual Gene Delivery System for the Synergistic Gene Therapy of Alzheimer's Disease. *ACS Nano* **2024**, *18*, 11753−11768.

(5) Wang, J.; Zhao, M.; Wang, M.; Fu, D.; Kang, L.; Xu, Y.; Shen, L.; Jin, S.; Wang, L.; Liu, J. Human Neural Stem Cell-Derived Artificial Organelles To Improve Oxidative Phosphorylation. *Nat. Commun.* **2024**, *15*, 7855.

(6) Jang, S. C.; Kim, O. Y.; Yoon, C. M.; Choi, D. S.; Roh, T. Y.; Park, J.; Nilsson, J.; Lötvall, J.; Kim, Y. K.; Gho, Y. S. Bioinspired Exosome-Mimetic Nanovesicles for Targeted Delivery of Chemotherapeutics to Malignant Tumors. *ACS Nano* **2013**, *7*, 7698−7710.

(7) Wang, X.; Hu, S.; Li, J.; Zhu, D.; Wang, Z.; Cores, J.; Cheng, K.; Liu, G.; Huang, K. Extruded Mesenchymal Stem Cell Nanovesicles Are Equally Potent to Natural Extracellular Vesicles in Cardiac Repair. *ACS Appl. Mater. Interfaces* **2021**, *13*, 55767−55779.

(8) Sun, M.; Yang, J.; Fan, Y.; Zhang, Y.; Sun, J.; Hu, M.; Sun, K.; Zhang, J. Beyond Extracellular Vesicles: Hybrid Membrane Nanovesicles as Emerging Advanced Tools for Biomedical Applications. *Adv. Sci.* **2023**, *10*, No. 2303617.

(9) Choo, Y. W.; Kang, M.; Kim, H. Y.; Han, J.; Kang, S.; Lee, J. R.; Jeong, G. J.; Kwon, S. P.; Song, S. Y.; Go, S.; Jung, M.; Hong, J.; Kim, B. S. M1Macrophage-Derived Nanovesicles Potentiate the Anticancer Efficacy of Immune Checkpoint Inhibitors. *ACS Nano* **2018**, *12*, 8977−8993.

(10) Wan, Y.; Wang, L.; Zhu, C.; Zheng, Q.; Wang, G.; Tong, J.; Fang, Y.; Xia, Y.; Cheng, G.; He, X.; Zheng, S. Y. Aptamer-Conjugated Extracellular Nanovesicles for Targeted Drug Delivery. *Cancer Res.* **2018**, *78*, 798−808.

(11) Moon, S.; Jung, M.; Go, S.; Hong, J.; Sohn, H. S.; Kim, C.; Kang, M.; Lee, B. J.; Kim, J.; Lim, J.; Kim, B. S. Engineered Nanoparticles for Enhanced Antitumoral Synergy Between Macrophages and T Cells in the Tumor Microenvironment. *Adv. Mater.* **2024**, *36*, No. e2410340.

(12) Ma, Q. L.; Fan, Q.; Xu, J. L.; Bai, J. Y.; Han, X.; Dong, Z. L.; Zhou, X. Z.; Liu, Z.; Gu, Z.; Wang, C. Calming Cytokine Storm in Pneumonia by Targeted Delivery of TPCA-1 Using Platelet-Derived Extracellular Vesicles. *Matter* **2020**, *3*, 287−301.

(13) Xu, X.; Xu, L.; Wen, C.; Xia, J.; Zhang, Y.; Liang, Y. Programming Assembly of Biomimetic Exosomes: An Emerging Theranostic Nanomedicine Platform. *Mater. Today Bio* **2023**, *22*, No. 100760.

(14) Lai, J.; Pan, Q.; Chen, G.; Liu, Y.; Chen, C.; Pan, Y.; Liu, L.; Zeng, B.; Yu, L.; Xu, Y.; Tang, J.; Yang, Y.; Rao, L. Triple Hybrid Cellular Nanovesicles Promote Cardiac Repair after Ischemic Reperfusion. *ACS Nano* **2024**, *18*, 4443−4455.

(15) Wang, K.; Zhang, X.; Ye, H.; Wang, X.; Fan, Z.; Lu, Q.; Li, S.; Zhao, J.; Zheng, S.; He, Z.; Ni, Q.; Chen, X.; Sun, J. Biomimetic Nanovaccine-Mediated Multivalent IL-15 Self-Transpresentation (MIST) for Potent and Safe Cancer Immunotherapy. *Nat. Commun.* **2023**, *14*, 6748.

(16) Liu, J.; Sun, Y.; Zeng, X.; Liu, Y.; Liu, C.; Zhou, Y.; Liu, Y.; Sun, G.; Guo, M. Engineering and Characterization of an Artificial Drug-Carrying Vesicles Nanoplatform for Enhanced Specifically Targeted Therapy of Glioblastoma. *Adv. Mater.* **2023**, *35*, No. e2303660.

(17) Wang, L.; Wang, G.; Mao, W.; Chen, Y.; Rahman, M. M.; Zhu, C.; Prisinzano, P. M.; Kong, B.; Wang, J.; Lee, L. P.; Wan, Y. Bioinspired Engineering of Fusogen and Targeting Moiety Equipped Nanovesicles. *Nat. Commun.* **2023**, *14*, 3366.

(18) Rao, L.; Wu, L.; Liu, Z.; Tian, R.; Yu, G.; Zhou, Z.; Yang, K.; Xiong, H.-G.; Zhang, A.; Yu, G.-T.; Sun, W.; Xu, H.; Guo, J.; Li, A.; Chen, H.; Sun, Z.-J.; Fu, Y.-X.; Chen, X. Hybrid Cellular Membrane Nanovesicles Amplify Macrophage Immune Responses against Cancer Recurrence and Metastasis. *Nat. Commun.* **2020**, *11*, 4909.

(19) Wiklander, O. P. B.; Mamand, D. R.; Mohammad, D. K.; Zheng, W.; Jawad Wiklander, R.; Sych, T.; Zickler, A. M.; Liang, X.; Sharma, H.; Lavado, A.; Bost, J.; Roudi, S.; Corso, G.; Lennaárd, A. J.; Abedi-Valugerdi, M.; Mäger, I.; Alici, E.; Sezgin, E.; Nordin, J. Z.; Gupta, D.; Görgens, A.; El Andaloussi, S. Antibody-Displaying Extracellular Vesicles for Targeted Cancer Therapy. *Nat. Biomed. Eng.* **2024**, *8*, 1453−1468.

(20) Mali, P.; Yang, L.; Esvelt, K. M.; Aach, J.; Guell, M.; DiCarlo, J. E.; Norville, J. E.; Church, G. M. RNA-Guided Human Genome Engineering via Cas9. *Science* **2013**, *339*, 823−826.

(21) Zhang, L.; Qin, Z.; Sun, H.; Chen, X.; Dong, J.; Shen, S.; Zheng, L.; Gu, N.; Jiang, Q. Nanoenzyme Engineered Neutrophil-Derived Exosomes Attenuate Joint Injury in Advanced Rheumatoid Arthritis via Regulating Inflammatory Environment. *Bioact. Mater.* **2022**, *18*, 1−14.

(22) Smyth, T.; Petrova, K.; Payton, N. M.; Persaud, I.; Redzic, J. S.; Graner, M. W.; Smith-Jones, P.; Anchordoquy, T. J. Surface Functionalization of Exosomes Using Click Chemistry. *Bioconjugate Chem.* **2014**, *25*, 1777−1784.

(23) Lou, S.; Ma, J.; Fu, P.; Li, L.; Huang, J.; Jing, F.; Wang, Y.; Qian, S.; Zheng, J.; Li, J.; Dong, Z.; Wang, K. Lung-Penetrating Biomimetic Extracellular Vesicle Spherical Nucleic Acids for Pulmonary Fibrosis Therapy through ROS Scavenging and Anti-Inflammatory Effects. *Aggregate* **2025**, No. e70086.

(24) Kundu, S.; Guo, J.; Islam, M. S.; Rohokale, R.; Jaiswal, M.; Guo, Z. A New Strategy to Functionalize Exosomes via Enzymatic Engineering of Surface Glycans and Its Application to Profile Exosomal Glycans and Endocytosis. *Adv. Sci.* **2025**, *12*, No. e2415942.

(25) Meng, W.; Wang, L.; Du, X.; Xie, M.; Yang, F.; Li, F.; Wu, Z. E.; Gan, J.; Wei, H.; Cao, C.; Lu, S.; Cao, B.; Li, L.; Li, L.; Zhu, G. Engineered Mesenchymal Stem Cell-Derived Extracellular Vesicles Constitute a Versatile Platform for Targeted Drug Delivery. *J. Controlled Release* **2023**, *363*, 235−252.

(26) Carney, R. P.; Mizenko, R. R.; Bozkurt, B. T.; Lowe, N.; Henson, T.; Arizzi, A.; Wang, A.; Tan, C.; George, S. C. Harnessing Extracellular Vesicle Heterogeneity for Diagnostic and Therapeutic Applications. *Nat. Nanotechnol.* **2025**, *20*, 14−25.

(27) Mishra, A.; Singh, P.; Qayoom, I.; Prasad, A.; Kumar, A. Current Strategies in Tailoring Methods for Engineered Exosomes and Future Avenues in Biomedical Applications. *J. Mater. Chem. B* **2021**, *9*, 6281−6309.

(28) Shi, M. M.; Yang, Q. Y.; Monsel, A.; Yan, J. Y.; Dai, C. X.; Zhao, J. Y.; Shi, G. C.; Zhou, M.; Zhu, X. M.; Li, S. K.; Li, P.; Wang, J.; Li, M.; Lei, J. G.; Xu, D.; Zhu, Y. G.; Qu, J. M. Preclinical Efficacy and Clinical Safety of Clinical-Grade Nebulized Allogenic Adipose Mesenchymal Stromal Cells-Derived Extracellular Vesicles. *J. Extracell. Vesicles* **2021**, *10*, No. e12134.

(29) Gao, Y.; Yuan, Z.; Yuan, X.; Wan, Z.; Yu, Y.; Zhan, Q.; Zhao, Y.; Han, J.; Huang, J.; Xiong, C.; Cai, Q. Bioinspired Porous Microspheres for Sustained Hypoxic Exosomes Release and Vascularized Bone Regeneration. *Bioact. Mater.* **2022**, *14*, 377−388.

(30) Dong, Z.; Liu, X.; Li, S.; Fu, X. Inhibition and Rescue of Hyperglycemia-Induced Cellular Senescence by Mitochondrial Transfer from Enucleated Mesenchymal Stem Cell-Derived Microvesicles for Chronic Wound Healing. *Adv. Sci.* **2025**, *12*, No. e01612.

(31) Chu, Q.; He, D.; Xie, W.; Li, S.; Dong, Z.; Fu, X. Gelated Microvesicle-Mediated Delivery of Mesenchymal Stem Cell Mitochondria for the Treatment of Myocardial Infarction. *Proc. Natl. Acad. Sci. U. S. A.* **2025**, *122*, No. e2424529122.

https://doi.org/10.1021/acsami.5c11126
ACS Appl. Mater. Interfaces 2025, 17, 54484−54495

(32) Yang, X.; Wang, Y.; Yang, Y.; Zhang, S.; Wang, D.; Luo, Y.; Shui, C.; Cai, Y.; Yang, R.; Dong, S.; Yang, M.; Lin, Y.; Li, C. Immunostimulatory DNA Tetrahedron-Based Nanovaccine Combined with Immune Checkpoint PD-1 Blockade for Boosting Systemic Immune Responses against Oral Squamous Cell Carcinoma. *Aggregate* **2025**, *6*, No. e70061.
(33) Shi, P.; Wang, X.; Davis, B.; Coyne, J.; Dong, C.; Reynolds, J.; Wang, Y. In Situ Synthesis of an Aptamer-Based Polyvalent Antibody Mimic on the Cell Surface for Enhanced Interactions between Immune and Cancer Cells. *Angew. Chem., Int. Ed.* **2020**, *59*, 11892−11897.
(34) Ye, T.; Liu, X.; Zhong, X.; Yan, R.; Shi, P. Nongenetic Surface Engineering of Mesenchymal Stromal Cells with Polyvalent Antibodies to Enhance Targeting Efficiency. *Nat. Commun.* **2023**, *14*, 5806.
(35) Park, J. H.; Jiang, Y.; Zhou, J. R.; Gong, H.; Mohapatra, A.; Heo, J. Y.; Gao, W. W.; Fang, R. H.; Zhang, L. F. Genetically Engineered Cell Membrane-Coated Nanoparticles for Targeted Delivery of active ingredient to Inflamed Lungs. *Sci. Adv.* **2021**, 7,No. eabf7820.
(36) Lai, C. P.; Mardini, O.; Ericsson, M.; Prabhakar, S.; Maguire, C.; Chen, J. W.; Tannous, B. A.; Breakefield, X. O. Dynamic Biodistribution of Extracellular Vesicles *In Vivo* Using a Multimodal Imaging Reporter. *ACS Nano* **2014**, *8*, 483−494.
(37) Wang, L.; Tang, Y.; Tang, J.; Liu, X.; Zi, S.; Li, S.; Chen, H.; Liu, A.; Huang, W.; Xie, J.; Liu, L.; Chao, J.; Qiu, H. Endothelial Cell-Derived Extracellular Vesicles Expressing Surface VCAM1 Promote Sepsis-Related Acute Lung Injury by Targeting and Reprogramming Monocytes. *J. Extracell. Vesicles* **2024**, *13*, No. e12423.
(38) Sanz, A. B.; Sanchez-Niño, M. D.; Ramos, A. M.; Ortiz, A. Regulated Cell Death Pathways in Kidney Disease. *Nat. Rev. Nephrol.* **2023**, *19*, 281−299.
(39) Tang, T. T.; Wang, B.; Li, Z. L.; Wen, Y.; Feng, S. T.; Wu, M.; Liu, D.; Cao, J. Y.; Yin, Q.; Yin, D.; Fu, Y. Q.; Gao, Y. M.; Ding, Z. Y.; Qian, J. Y.; Wu, Q. L.; Lv, L. L.; Liu, B. C. Kim-1 Targeted Extracellular Vesicles: A New Therapeutic Platform for RNAi to Treat AKI. *J. Am. Soc. Nephrol.* **2021**, *32*, 2467−2483.

https://doi.org/10.1021/acsami.5c11126
ACS Appl. Mater. Interfaces 2025, 17, 54484−54495